Noname manuscript No.
(will be inserted by the editor)

A single-camera synthetic Schlieren method for the measurement of free liquid surfaces

Huixin Li, Marc Avila and Duo Xu

Received: date / Accepted: date

Abstract A single-camera synthetic Schlieren method is introduced to measure the height of a dynamic free liquid surface in a container with a flat bottom. Markers placed on the bottom, seen through the free surface, are virtually displaced due to light refraction at the surface. According to Snell's law, the marker displacements depend on the refractive indices of the transparent liquid and the air, and on the surface height and its spatial gradients. We solve the resulting governing nonlinear equation with the Newton–Raphson method to obtain the surface height. Our method does not require a reference surface height, which allows the measurement of surfaces topography in situations where the liquid depth is unknown. We demonstrate the accuracy of the method by performing experiments of surface ripples and dam-break flows, and discuss the measurement uncertainty, errors and limitations.

Keywords surface topography · height of free surface · synthetic Schlieren · single camera

Huixin Li
University of Bremen, Center of Applied Space Technology and Microgravity (ZARM), 28359 Bremen, Germany

Marc Avila
University of Bremen, Center of Applied Space Technology and Microgravity (ZARM), 28359 Bremen, Germany

Duo Xu
The State Key Laboratory of Nonlinear Mechanics, Institute of Mechanics, Chinese Academy of Sciences, 100190 Beijing, China
School of Engineering Science, University of Chinese Academy of Sciences, 100049 Beijing, China
University of Bremen, Center of Applied Space Technology and Microgravity (ZARM), 28359 Bremen, Germany
E-mail: duo.xu@imech.ac.cn (Corresponding author)

1 Introduction

The quantitative measurement of a liquid free surface is fundamentally important in many applications. For example, in marine and coastal engineering, wind-generated surface waves have substantial impacts on marine vessels and offshore platforms (Holthuijsen, 2007). In chemical engineering, falling liquid films with dynamic free surface are employed for the efficient heat exchange in steam condensers (Karimi and Kawaji, 1998). The liquid sloshing with dynamic free surface motions are essential in propellant tank in aerospace devices and in liquid natural gas cargos in ship industry (Ibrahim, 2005). Quantitative optical imaging measurements of the height of the free surface are advantageous because of their non-intrusive nature.

One imaging methodology associates the height of the free surface with light absorption in the liquid. Given that image magnification is independent of surface height, Jähne et al. (2005) used a telecentric optical system to measure the surface height, which is a function of the light absorption rates from light-emitting diodes (LEDs) with red and near-infrared lights. Here a challenging task is to precisely align the collimated beams in different wavelengths. Aureli et al. (2014) used a camera with two charged-coupled devices (CCDs) including a monochrome near-infrared sensor in order to implement the surface measurements with the working principle of light absorption. They took the advantage of high absorption capacity of water in the near-infrared range. Their method can reach an accuracy in the order of 1 mm, however the measurement sensitivity decreases with the water depth.

Planar laser-induced fluorescence (LIF) with a laser sheet has also been used to capture the profiles of the free surface (Duncan et al., 1999; André and Bardet, 2014). A fast-scanning of a laser sheet can be used to obtain and reconstruct the surface topography in two dimensions (van Meerkerk et al., 2020). The scanning needs to be fast enough so that the surface structure can be approximately assumed to be frozen. In the LIF method, edge-detection algorithms are required to extract the surface profiles from the LIF images, and the physical length corresponding to an image pixel determines the measurement resolution. The measurement dynamic range (the ratio of the maximum measured value to the smallest measured value) is determined approximately by the image resolution.

Light reflection can also be used for surface measurements. For example, the slope of two-dimensional surfaces can be measured with a polarimeter by correlating the surface orientation with changes of light polarization (Zappa et al., 2008). This technique can be used not only in laboratory but also in rivers with unpolarized skylight or moon-glade (Zappa et al., 2008; Vinnichenko et al., 2020). Alternatively, symbol patterns and fringe patterns are projected onto the surface, and the deformation of the patterns due to the surface topography is exploited for the surface measurements (Tsubaki and Fujita, 2005; Cobelli et al., 2009; Hu et al., 2015). The intensity of the light reflection is crucial to the measurement accuracy, and additives mixed with the liquid (water) are employed to improve the light reflection at the surface.

A group of imaging techniques relies on light refraction. Kurata et al. (1990) used a camera to capture a reference and a refraction image of a striped grating, which was placed below a shallow water channel. When the water surface had ripples, the imaged grating was virtually displaced with respect to the still, horizontal water

surface, due to the changed light refraction. In their method, the topography of the free surface is obtained from the virtual displacements. The surface height can also be obtained provided that the height of a reference surface point is known. In their flow, there is a point that the surface height is nearly unchanged in time, so that they use the height at this point as the reference height to reconstruct the surface depth from the topography data. Fouras et al. (2008), Moisy et al. (2009) and Ng et al. (2011) further developed this method by replacing the grating with random dot patterns, so that optimized cross-correlation particle-image-velocimetry (PIV) algorithms can be used to compute the virtual displacements precisely. Alternatively to the dot patterns, Zhang and Cox (1994) introduced a color-coded pattern, where colors were designed to correlate with surface slopes one-to-one (Dabiri et al., 1997).

The advantages of refraction methods are the use of low-cost illumination, simple optical configuration and a single camera. Despite their simplicity and precision, a drawback of these methods is that a reference height is needed to reconstruct the height of the surface from the surface topography. In some situations, the liquid depth is not known and the method cannot be applied. Morris (2004) and Gomit et al. (2013) used two or more cameras to obtain stereoscopic views of the same pattern. They could directly obtain the topography and the height of the free surface by matching the surface orientation at each surface point from the measurements of multiple cameras (Morris, 2004) (see table 1). However, using multiple cameras raises the hardware costs, results in more time-consuming calibration of the camera positions, and requires more computation power in the post-processing. Recently, Engelen et al. (2018) proposed a method with a single camera for the surface measurements, which relies on the condition that the surface topography can be depicted by a parametric model.

We present an extension of the free-surface synthetic Schlieren (FS-SS) method of Moisy et al. (2009), which allows to directly measure the topography and the height of the free liquid surface using a single camera, without neither reference height nor parametric models. In §2, the working principle is introduced. Two sets of experiments were carried out to test our method. Experiments of surface ripples, where the spatially averaged height is approximately constant, are shown in §3. Experiments of dam-break flows, where the averaged height changes in time, are presented in §4. A detailed discussion and conclusions are given in §5 and §6, respectively.

2 Methodology

The presented methodology exploits the light refraction at the air-liquid interface. A schematic of the working principle, based on the synthetic Schlieren method (Moisy et al., 2009) and the background-oriented Schlieren method (Raffel, 2015), is shown in figure 1. When there is no liquid, the incident light ray at a point P follows a straight trajectory (shown in black) toward the camera. When there is a liquid-air interface, the incident light ray at point P' follows the dashed gray trajectory toward the surface and then follows the same black trajectory after leaving the surface. The light refraction is governed by the Snell's law for refractive index of the liquid n_l and that of the gas n_a (in this study $n_l = 1.334$ and $n_a = 1$, corresponding to water

Reference	Quantity of camera	Method	Object & pattern	Illumination	Measurability of liquid height
Zhang and Cox (1994)	1	Refraction	Random colored blocks	Halogen light	Yes, with reference height
Dabiri et al. (1997)	1	Refraction / Reflection	Random colored blocks	–	Yes, with reference height
Morris (2004)	2	Refraction & pattern	Checkerboard	LED	Yes
Jähne et al. (2005)	1	Refraction & light absorption	Gridded dots	LED	Yes, with complex telecentric illumination
Fouras et al. (2008)	1	Refraction & Image correlation	Random dots	LED	Yes, with reference height
Moisy et al. (2009)	1	Refraction & Image correlation	Random dots	LED	Yes, with reference height
Gomit et al. (2013)	3	Refraction	Random PIV tracers	Laser sheet	Yes
Aureli et al. (2014)	1	Refraction & light absorption	Random colored blocks	LED	Yes, with coupled RGB Bayer array and Monochrome sensor
Engelen et al. (2018)	1	Refraction & pattern match	Checkerboard	LED	Yes, with parametric surface model
Kolaas et al. (2018)	2	Refraction & image correlation	Random dots	bichromatic LED	Yes, with reference height and telecentric lens

Table 1 A brief list of refraction methods for free surface measurements.

and air). The displacement $\delta\mathbf{r}$ from the point P to the point P' depends on the liquid height $h(x,y)$, and its spatial gradients $\nabla h(x,y)$, according to the equation

$$\delta\mathbf{r} = h\left[\tan\left(\tan^{-1}(\nabla h) + \sin^{-1}[(n_a/n_l)\cdot\sin(\boldsymbol{\beta} - \tan^{-1}(\nabla h))]\right) - \tan(\boldsymbol{\beta})\right], \qquad (1)$$

where $\boldsymbol{\beta} = \beta_x(x,y)\hat{x} + \beta_y(x,y)\hat{y}$ denotes the angle of the camera viewing the point P. The detailed derivation of this equation is given in Appendix. When the camera is set to satisfy the paraxial approximation, $\boldsymbol{\beta}(x,y)$ is small so that $\tan(\boldsymbol{\beta}) \approx \boldsymbol{\beta}$. Similarly, $\tan(\nabla h) \approx \nabla h$ when ∇h is small, e.g. $\nabla h < 0.5$, see §5.5. Then equation (1) can be simplified to

$$\delta\mathbf{r} = h\cdot(1 - n_a/n_l)\,(\nabla h - \boldsymbol{\beta}), \qquad (2)$$

where $h(x,y)$ is the only unknown to be determined, provided that $\delta\mathbf{r}$ and $\boldsymbol{\beta}$ have been pre-computed, as explained in what follows.

The displacement $\delta\mathbf{r}(x,y)$ can be obtained by taking the cross-correlation operation over the reference and the refraction images of dot objects (see figure 2b, c). Image cross-correlation algorithms, as commonly used in two-dimensional PIV, are

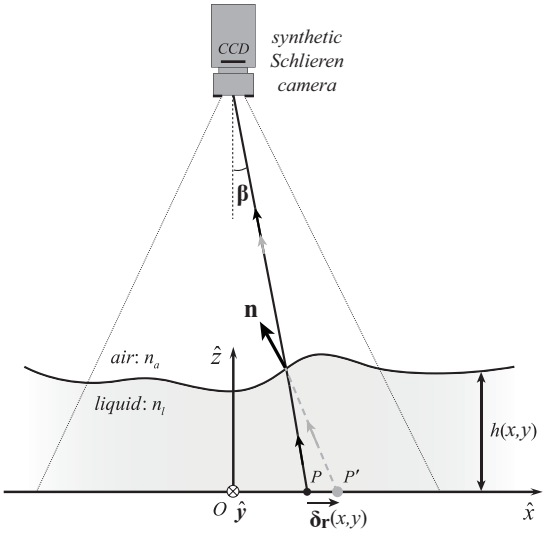

Fig. 1 Schematic of working principle of measuring the topography and the height of free air-liquid surface $h(x,y)$ with a surface normal direction $\mathbf{n}$. $(\hat{x},\hat{y},\hat{z})$ and O denote the Cartesian coordinate and the origin, respectively. The displacement from a point P to the point P' (due to the surface refraction) is $\delta\mathbf{r}$. $\boldsymbol{\beta}$ is the angle between the light (black line with an arrow) and the camera axis.

applied in this study. In this study, the multi-step algorithm is used with interrogation window 96×96 pixel^2 at the initial step reducing to the window 24×24 pixel^2 with 75% window overlap at the final step, an optimized setting in Lavision Davis©. The interrogation window at the final step includes approximately 8 dots for accurate displacement tracking (Raffel et al., 2018), given that the number of dots in each interrogation window between the paired images is approximately unchanged. In this work, the dot objects are printed (randomly distributed) on a transparent sheet. The random distribution of the dots helps the PIV correlation algorithm reduce fortuitous pattern coincidence and renders better accuracy. We carefully designed the pattern, where the diameters of individual dots are approximately 5 to 6 pixels in images.

The camera viewing angles, $\boldsymbol{\beta}(x,y) = \beta_x(x,y)\hat{x} + \beta_y(x,y)\hat{y}$, are determined by the spatial position of the camera to the object pattern (e.g. see figure 2a), and can easily obtained in a calibration procedure. For a leveled flat bottom and a still (flat) water surface (i.e. $\nabla h = 0$, known n_l), the surface height h_c can be measured with a caliper precisely. According to equation (2), $\boldsymbol{\beta}(x,y) = -\delta\mathbf{r}_c(x,y)/[h_c(1-n_a/n_l)]$ with $\delta\mathbf{r}_c(x,y)$ obtained from the cross-correlation operation. Note that the height h_c can be freely chosen and does not depend on the details of the experiments (e.g. water fill level) to be performed in the tank.

We solve for $h(x,y)$ in equation (1) and (2) using the Matlab intrinsic function *fsolve* (Levenberg–Marquardt algorithm), which requires long computing time and large memory. To reduce the need of computation power and time, an *in-house* Matlab code implementing the Newton–Raphson method was scripted to solve the equation (2). The gradient ∇h is discretized with central, second-order finite differences

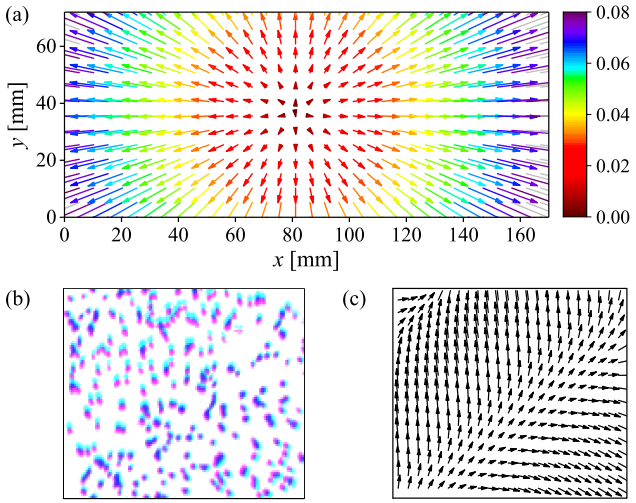

Fig. 2 (Color online) (a) The vector map of $\boldsymbol{\beta}(x,y)$ obtained in the calibration procedure, where the direction of a vector is given by β_x and β_y, and the color shows the magnitude $|\boldsymbol{\beta}|$. Every other vector along each direction is shown for clarity. (b) A portion of dot pattern is shown: pink dots (tuned from black) are from a calibration image, while cyan dots (tuned from black) are from a measurement image of surface ripples, and the overlap is in blue. (c) The displacements $\delta\mathbf{r}$ (amplified 4 times in length for clarity) between the pink and the cyan dots in (b).

at interior grid points and with forward/backward second-order differences at the boundaries. The displacements $\delta\mathbf{r}(x,y)$ span $M \times N$ grid points, and at each grid point there are two components of $\delta\mathbf{r}$ and one h. This leads to a linear system including $2MN$ equations and MN unknowns. This over-determined linear system can be solved without imposed boundary conditions by Newton iterations from an initial guess (a positive constant) to the converged solution $h(x,y)$. Convergence is assured if the maximum of the least-squared residual errors in the linear system drops below 10^{-5}.

We note that $\delta\mathbf{r}$ is measured with respect to the point P in figure 1, whereas the coordinates of the intersection (surface) point for the solved h differ from P. The coordinates of the solved $h(x,y)$ thus need to be remapped according to $(x,y)^* = (x,y) - h(x,y)\tan[\boldsymbol{\beta}(x,y)]$.

3 Liquid ripples

In this section, we report on experiments of surface ripples, where the spatially averaged surface height is approximately constant.

3.1 Experiments

The tank that was manufactured with transparent acrylic plates has dimensions of $1000 \times 150 \times 350\ \mathrm{mm}^3$ in length, width and height. The random dot pattern in dimen-

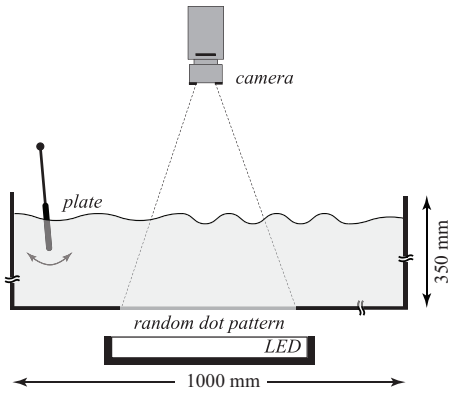

Fig. 3 Schematic of measuring topography and height of liquid ripples in a tank. The dimensions are not in scale.

sion of 200 mm $\times$ 120 mm was printed on an overhead transparency (in thickness of 0.16 mm) in a printer (Ricoh MP C3504). The dot pattern was attached upon the inner flat bottom of the tank. A white LED with a light diffuser was applied to illuminate the dot pattern from the bottom of the tank, while a camera (Phantom VEO 640L equipped with a Zeiss lens of focal length 100 mm) in resolution 2560 $\times$ 1600 pixel^2 was placed approximately 1 meter above the pattern. A plate was employed to flap back and forth to generate surface ripples (see figure 3).

The experiments were carried out in the following order. The tank bottom was leveled; An image was captured as the reference image I_0 when there was no water in the tank; The water was filled into the tank to a height of 20 ± 0.1 mm which was measured by a caliper, and an image I_{h_0} was captured when the water surface was still. When the water ripples were generated, a series of images $I(t)$ was recorded.

When the images $I(t)$ are correlated with the image I_0 to get $\delta\mathbf{r}(x,y,t)$, the equation (1) is solved to give $h(x,y,t)$ from the present method. For comparison, when the images $I(t)$ are correlated with the image I_{h_0} to get the displacements, $h(x,y,t)$ can be obtained with the FS-SS method (Moisy et al., 2009). The script of FS-SS method of Moisy et al. (2009) was downloaded from their website and compared with our script of the FS-SS method to confirm that we understand their method correctly. In their script, the solution of the topographic height at the bottom left point of the computation domain is set to be zero, then the summation of the solved topographic height and the reference height gives the surface height.

3.2 Results

A snapshot of the surface ripples measured with our method is shown in figure 4(b), and it is visually in good agreement with the result of the FS-SS method shown in (a). This comparison is performed on the surface topography by removing the spatially averaged height $\overline{h}(t)$ from $h(t)$. The particular consideration behind this comparison is that, although the reference height h_0 is constant, the averaged height within the

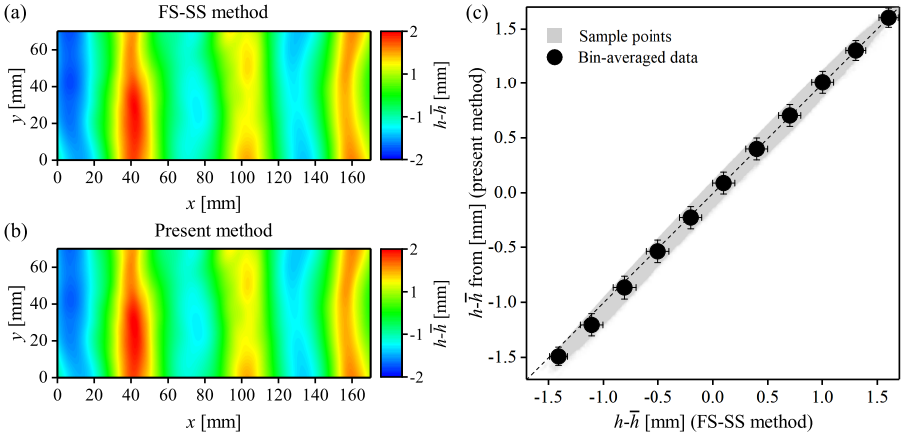

Fig. 4 (Color online) The contours of topography from the FS-SS method (a) and from our method (b). (c) Comparison of $h-\overline{h}$ between present method and FS-SS method in experiments of dynamic ripples, where the gray squares denote individual data in space. A black dot shows the average of the individual points in a bin with the size of 0.3 mm, and an error bar shows the standard deviation of the data in the bin.

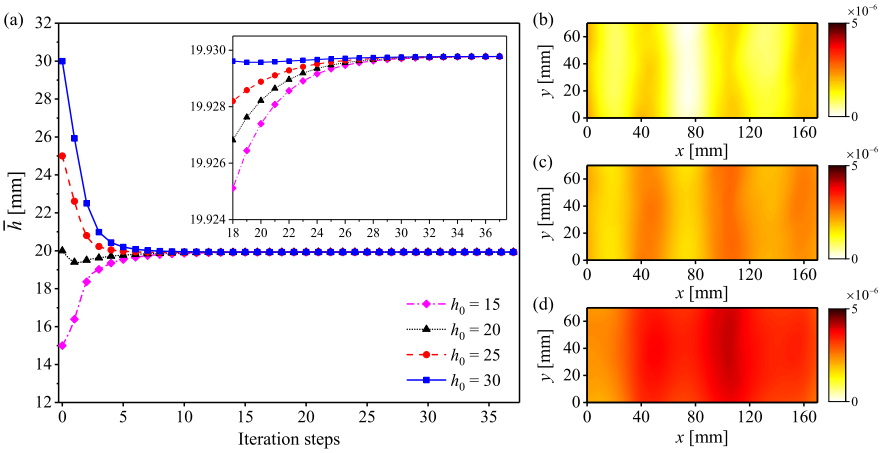

Fig. 5 (Color online) The effects of initial guesses in Newton method on $h(x,y)$ in solution. (a) The mean height $\overline{h}$ resulted from initial guesses $h_0 = 15, 20, 25, 30$ against iteration steps, where the inset shows a zoom for iteration steps larger than 18. (b–d) The contours of topography differences, $h(x,y,h_0 = 30) - h(x,y,h_0 = 20)$, $h(x,y,h_0 = 25) - h(x,y,h_0 = 20)$ and $h(x,y,h_0 = 15) - h(x,y,h_0 = 20)$, respectively.

field-of-view measurements may vary temporally, which may break the fundamental assumption of the FS-SS method (Moisy et al., 2009). About $8,000,000$ individual spatial points of $h(x,y) - \overline{h}(x,y)$ from 200 temporal snapshots are shown as the gray squares in figure 4(c), where a black dot shows the bin-averaged value of the individual points. Good quantitative agreement between the two methods is obtained.

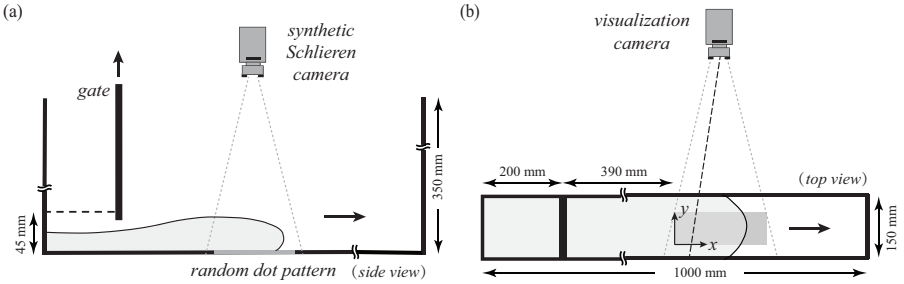

Fig. 6 (a) Side view schematic of a lock-exchange experimental setup for propagation of current fronts in a dam-break flow. The camera and illumination systems are the same as in figure 3. (b) Top-view schematic of visualization measurements. The thick black arrow indicates the flow direction, and the gray rectangular marks the area where $h(x,y)$ is measured. The dot lines enclose the field-of-view of the visualization camera, and the dash line marks the perspective view of the camera. The dimensions are not in scale.

3.3 Effect of initial guesses

The effect of initial guesses for the Newton-Raphson method on the computed $h(x,y)$ is shown in figure 5(a). For the same snapshot shown in figure 4(b), the spatially averaged heights $\overline{h}$ computed from initial guesses $h_0(x,y) = 15, 20, 25, 30$ converge to the same value $\overline{h} \approx 19.93$ (see the inset). The contours of the topographic difference on $h(x,y)$ between the result with $h_0 = 20$ (shown in figure 4b) and those with other initial guesses are shown in figure 5 (b–d), where the difference is only about 10^{-6}. This shows that the present method does not depend on different initial guesses. When the initial guesses are meaningful, i.e. $h_0 > 0$, the present method does not have multi-solution issues as reported in Gomit et al. (2013). In practice, we suggest to take $h_0(x,y)$ slightly larger than the maximum height of the surface from *a-priori* knowledge of the flow.

4 Dam-break problem: propagation of a current

A dam-break problem involves a liquid current propagating downstream with the averaged height temporally changing. The experiments of the dam-break problem introduced in this section demonstrate that with our method flows with temporally evolving averaged height can be measured.

4.1 Experiments

The experiments of the dam-break problem were carried out in a lock-exchange setup as sketched in figure 6(a). The tank is the same as used in the experiments of the liquid ripples. The experimental procedure is as follows. Water was filled into the locked portion of the tank only (the left side of the gate) to the height marked by a dashed

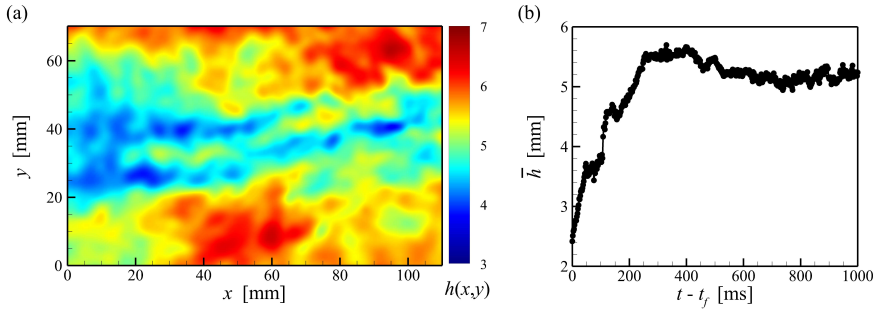

Fig. 7 (Color online) (a) Contours of a sample $h(x,y)$ of the current body at $t-t_f = 234$ ms. (b) Time series of $\bar{h}$ for the current body, where $t_f(= 152$ ms) is time duration of the current front passing the measurement domain. The gate is opened at $t \approx -40$ ms.

line (45 mm in height); The gate was rapidly, manually moved away vertically, and the water flowed into the right side of the gate driven by gravity formed a dynamical current.

The dot pattern was attached to the inner bottom of the tank, while a camera was placed approximately 1.5 m above the bottom (see figure 6a). The details of the camera-illumination system are given in §3. An example of the current body, the surface height upstream of the current front is shown in figure 7(a), where large spatial variations of the current heights can be observed. In time, the averaged current height $\bar{h}$ changes by 3 mm in a short time interval (300 ms). As consequence, the FS-SS method is inapplicable in this flow condition.

4.2 Measurement validation

For validation purposes, a visualization system was additionally set up to capture the height profile of the current at the same time. The visualization camera (also a Phantom VEO 640L) was placed approximately 0.7 m away from a sidewall of the tank. A white paper was attached outside another sidewall of the tank to produce an approximately uniform background. Every liter of water was premixed with 18 ml ink to increase the contrast of the imaged current to the background. The visualization was with illumination from the same LED as the synthetic Schlieren measurement. This visualization measurement approximately captures the surface height averaged in the y direction (see details below). The two cameras were synchronized and the sampling rate of the measurements was 500 frames per second. The measurement domain of the free surface was 110×70 mm in streamwise and spanwise direction, respectively. The upstream border of the measurement domain was about 390 mm downstream of the gate.

The height profile of the current body was obtained from the visualization measurements as follows. An image of the standard deviation (at each pixel) (see fig-

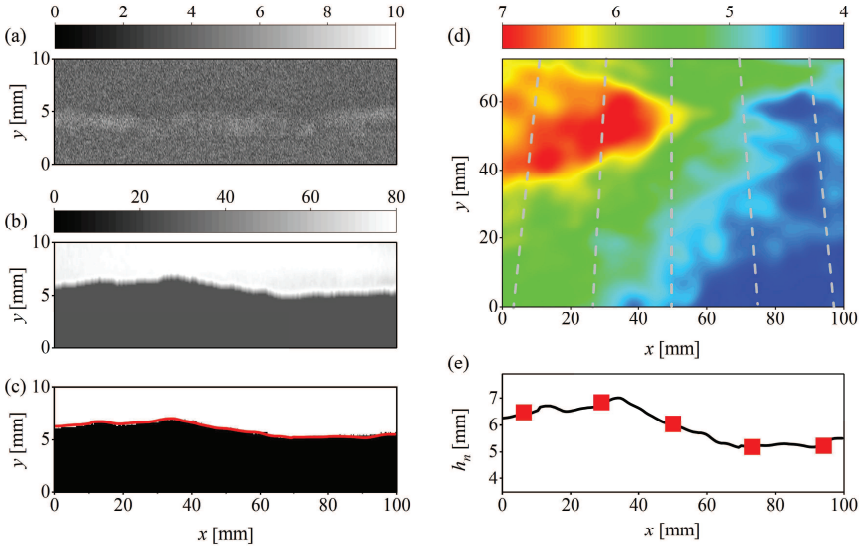

Fig. 8 (Color online) Illustration of the image processing in the visualization measurement: (a) The image of the standard deviation of the background images; (b) A sample of visualization image; (c) The tuned image with marking the pixel with grayscale larger (or smaller) than three times of the standard deviation as black (or white), where a red line marks the height profile. Illustration of obtaining $h_n(x)$ (e) from $h(x,y)$ (d), where dashed lines indicate the perspective direction and five red squares denote the data from the five dashed lines.

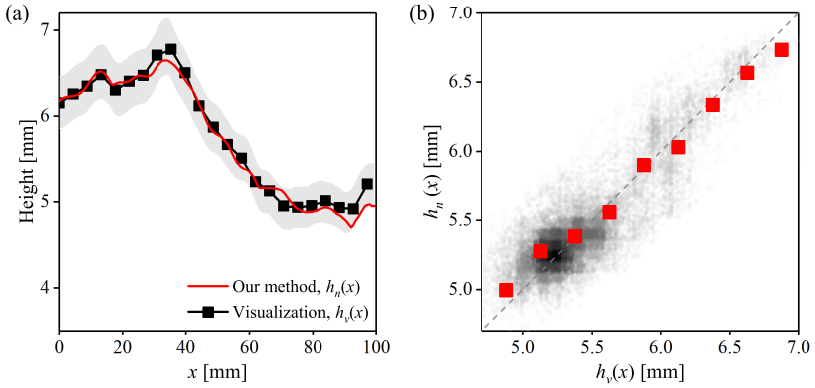

Fig. 9 (Color online) Comparison of streamwise profiles of current body between the visualization and our method. (a) The streamwise profiles $h_v(x)$ (visualization) and $h_n(x)$ (present method) along the streamwise direction x. Gray band show the error bar of visualization measurement. (b) $h_n(x)$ versus $h_v(x)$, where individual data are shown in points and the grayscale level indicates the probability density function (pdf) (the darker the larger pdf), and red squares show the bin-averaged data.

ure 8a) and an image of the averaged background were obtained from the background images captured before the experiments (i.e. without liquid in the measurement region). A visualization image of the current body is shown in figure 8(b). For the visualization image with removal of the averaged background image, if the absolute value at the pixel is larger than three times of the standard deviation at the pixel, it indicates that water flows over the pixelwise region, and the pixel is marked as black (see figure 8c). Similarly, if the absolute value at the pixel is smaller than three times of the standard deviation at the pixel, no water flow is expected and the pixel is marked as white (see figure 8c). The height profile of the current is given by the borders between the white and the black regions, then a 3-point moving average operation was used to smooth the profile to give $h_v(x)$ for the visualization measurements (see figure 8c).

The visualization camera has a perspective view of the flow, and a point of the height profile approximately corresponds to the maximum height along a perspective line (see e.g. the dash line in figure 6b). Thus, for better comparison with the height profile of the visualization measurement, $h(x,y)$ from our synthetic Schlieren method is post-processed. 100 points are defined with equidistance in the streamwise length of the field-of-view of the visualization camera, and they are connected to the position point of the visualization camera to define 100 perspective lines (see examples of 5 perspective lines, the dashed lines in figure 8d). The surface height $h(x,y)$ is interpolated along the 100 perspective lines, and the maximum value along each perspective line is obtained to give $h_n(x)$.

We then compare $h_n(x)$ and $h_v(x)$ in figure 9(a), and they approximately collapse. About $24,000$ points of the current profiles from about 180 snapshots are shown as gray dots in figure 9(b), where the red squares show the bin-averaged data. The two measurement results agree with small differences, which are mainly from two aspects: (1) The data of two measurements are from different sizes of the measurement domain. Although a black mask was used to block the area outside the gray rectangular in figure 6(b), the perspective illumination made the visualization measurement domain slightly larger than the measurement domain from the present method. (2) The visualization measurements are affected by the light reflection at the free surface and the spatially inhomogeneous illumination intensity which varies in time. Consequently, the current profiles from the visualization measurements have larger uncertainties.

4.3 Dynamics of current front

The sharp fronts where the height changes abruptly ($\nabla h \gg 1$) in a short streamwise distance (see figure 10a) results in an ill-conditioned Jacobian matrix of the Newton-Raphson method. This leads to height errors at the downstream region of the front edge, where the height should be zero. We found that imposing a Dirichlet boundary condition at the downstream border of the computation domain (i.e. $h(\max(x),y) = 0$) can remedy this issue. In addition, occasionally in some snapshots, downstream of the fronts, there are spike-like structures possibly given by numerical noise (height of about 0.5 mm, see figure 10b), the cause of which is unclear. The dynamics of the

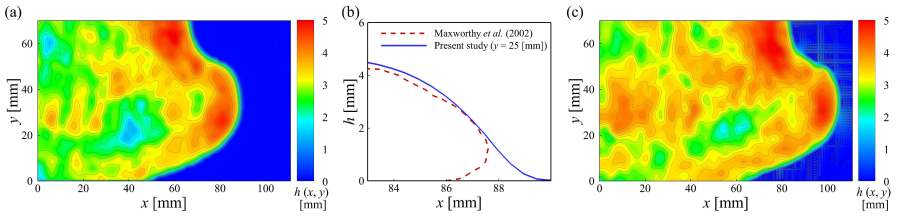

Fig. 10 (a) Contours of a sample of the current front with no numerical noise. (b) The height profile of the current front, where the blue solid line shows the profile at $y = 25$ mm in (a). The red dashed line shows a typical profile of a gravity current, which is extracted from the top panel of figure 4 in Maxworthy et al. (2002), and the values are adjusted to shown in the same figure. (c) Contours of a sample of the current front with spike-like numerical noise downstream of the front.

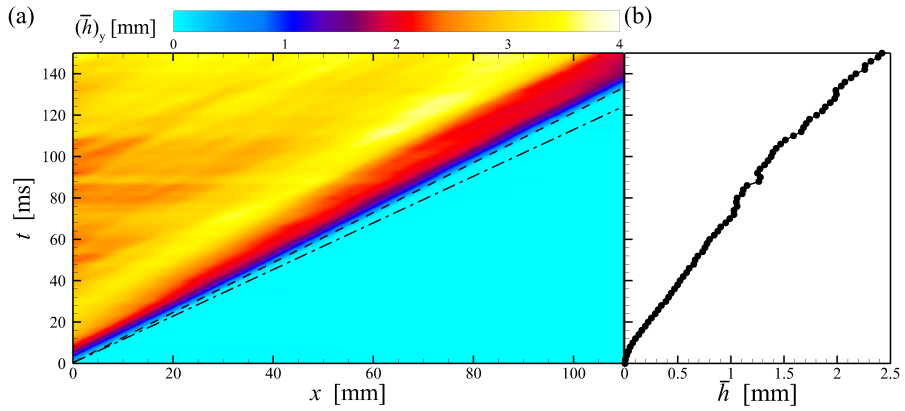

Fig. 11 (Color online) (a) Spatio-temporal diagram of the current fronts, where the color indicates the $h(x,y)$ averaged over y, $(\bar{h})_y(x) = \sum_{i=1}^{N} h(x,y_i)/N$. The dash line indicates the front speed in our experiments. The front speed of Lowe et al. (2005) is nearly the same as our experiments and is also denoted by this dash line. The dash-dot line indicates the front speed of Adegok et al. (2014). (b) The corresponding spatial averaged height $\bar{h}(t)$, in sharing the same axis t.

current front (after removing the noise downstream of the front) and the body can be seen in a supplemental movie.

In figure 10(a), a region of large height $h \approx 5$ mm can be seen close to the front, downstream of which the height decreases to about 3 mm with large spatial fluctuations. This experimental scenario agrees with the simulations of Shin et al. (2004); Borden and Meiburg (2013). However, a difference on the structures of the front interface can be observed (and is expected) in figure 10(b). This difference is due to the breakdown of the working principle in this region (see the discussion in §5.4). We then show the spatio-temporal diagram of the current front in figure 11(a). The dash line marks the position of the current front at times, and a constant propagation speed can be seen. The front speed in our experiment is approximately 0.82 m/s. This agrees well with the result of Lowe et al. (2005) (about 0.83 m/s) and Adegok et al. (2014); Lauber and Hager (1998) (about 0.9 m/s). In the measurement domain, the

averaged height changes in time, i.e., it increases from 0 to approximately 2.4 mm (see figure 11b).

5 Discussion

Equation (2) has a simple form, and can be solved fast for a case using our Matlab code. This is ideal for performing the uncertainty and error analysis, as well as deriving the critical condition when the working principle is broken, thus equation (2) is used for solving the surface height in this section.

5.1 Measurement uncertainty from cross-correlation methods

The presented method relies on computing the displacements of dots of a pattern via a cross-correlation method. In the present study, the configuration of the interrogation windows of size decreasing down to 24×24 pixel^2 with 75% overlap (a suggested setting in Lavision Davis), and a sub-pixel Gaussian interpolation was used (Raffel et al., 2018). The uncertainty is expected to be around 0.1 pixel and smaller, because the random dot pattern was generated to satisfy an optimal PIV condition (Moisy et al., 2009). In our problem, the uncertainty on each component of displacements of an instantaneous sample is up to about 0.05 pixel (from Lavision Davis©, see Wieneke (2015)).

To investigate the uncertainty of the cross-correlation method on the measured surface height, the uncertainty propagation in a linear system cannot be applied to the equation (1) (or 2). Instead, random noise was added to two components of displacement fields to evaluate the uncertainty. Two types of noises were examined: Gaussian distribution with a mean of 0.1 pixel and a standard deviation of 0.05 pixel, where signs ($+$ or $-$) of the values are randomly chosen; white noise (ranging from -0.15 pixel and 0.15 pixel). The contaminated displacements were used to calculate the surface height $\hat{h}(x,y)$, and the resulted difference is $\hat{h}(x,y) - h(x,y)$. This procedure was repeated 100 (Gaussian) $+100$ (white) times, and for each time the noise was randomly generated.

For the data shown in figure 4 (c), the relative uncertainty averaged over space and 100 noise samples is approximately 0.2% in average with a standard deviation of 1.2% for the Gaussian noise, and 0.1% in average with a standard deviation of 0.9% for the white noise.

The same method of the uncertainty estimation was also applied to a displacement field, which was numerically generated in equation (2) with $h = 0.5\sin(0.1x + 0.08y) + 10$ (simulating ripple stripes). For the Gaussian noise, the mean relative error is -0.3% with a standard deviation of 2%, while the mean relative error is nearly zero with a standard deviation of 1.4% for the white noise.

Interrogation window [pixel^2]	$\max(h)-\min(h)$ [mm]	$\max(\|\|\nabla h\|\|)$	$\overline{h}$ [mm]
24×24 (0% overlap)	0.921	0.165	9.666
48×48 (0% overlap)	0.882	0.116	10.214
96×96 (0% overlap)	0.852	0.063	10.189

Table 2 The effect of interrogation window size on the surface height and topography of the snapshot in figure 4(c).

5.2 Effect of camera vibration

The measurements using our method are sensitive to camera vibration. In our preliminary set-up, the camera vibration was particular evident and it was possibly from the cooling fan of the high-speed camera, as reported elsewhere (Moisy et al., 2009), or the vibration of the supporting profiles for the camera. The vibration produced approximately 0.2 pixel in images of a still target, and the vibration was mainly along y direction in the images. To evaluate the effect of the camera vibration on surface height, a noise taking the form $\delta\mathbf{r}_{\text{vibration}}(x,y)=\mathrm{c_r}\cdot y+\mathrm{c_t}$ is employed to mimic rotation ($\mathrm{c_r}$) and translation ($\mathrm{c_t}$) of the camera in vibration. $\delta\mathbf{r}_{\text{vibration}}$ is then added to the measured $\delta\mathbf{r}$ to compute $h(x,y)$. The combination of $-3\times 10^{-4}\leqslant \mathrm{c_r}\leqslant 3\times 10^{-4}$ and $-0.2\leqslant \mathrm{c_t}\leqslant 0.2$ (in pixel) gives vibration displacement up to 0.4 (pixel). Taking a measurement sample of $\overline{h}\approx 10$ as an example (as seen in table 3 in appendix), the mean height ranges from 9.3 to 13, producing the relative error up to approximately 30% (see table 4 in appendix).

Particular care is therefore necessary to stabilize the camera against vibrations. If the vibration remains intolerable, measuring the vibration simultaneously with the surface height is necessary. For instance, the border or the corner region in the field-of-view of a camera can be used to record still objects without any light refraction, while the center region of the frame can be used to measure the marker displacements for the surface height. The shifts of the still targets can be then taken for evaluation of the camera vibration, e.g. through a two-dimensional linear interpolation (with assumed form $\delta\mathbf{r}_{\text{vibration}}(x,y)=\mathrm{c_r}\cdot y+\mathrm{c_t}$). The $\delta\mathbf{r}_{\text{vibration}}(x,y)$ needs to be removed from $\delta\mathbf{r}(x,y)$ before the Newton-Raphson computation.

5.3 Effect of resolution

The spatial resolution of the displacement $\delta\mathbf{r}(x,y)$ plays a key role for measurements of $h(x,y)$. The dynamic range of surface topography wavelengths is determined approximately by the dynamic range of $\delta\mathbf{r}$. To examine the effect of resolution, a pair of images was processed with the interrogation window size of 24^2 pixels^2 up to 96^2 pixels^2 and 0% overlap was used. As shown in table 2, as the resolution is decreased (increase of window size), the topographic structures are smoother and more flat, given by the decrease of $\max(||\nabla h||)$ and the decrease of $\max(h)-\min(h)$, respectively, and the averaged height is correspondingly changed.

The two-dimensional power spectrum was calculated for $h(x,y)-\overline{h}$ to examine the fluctuations of the heights, and the radially averaged power spectrum is shown

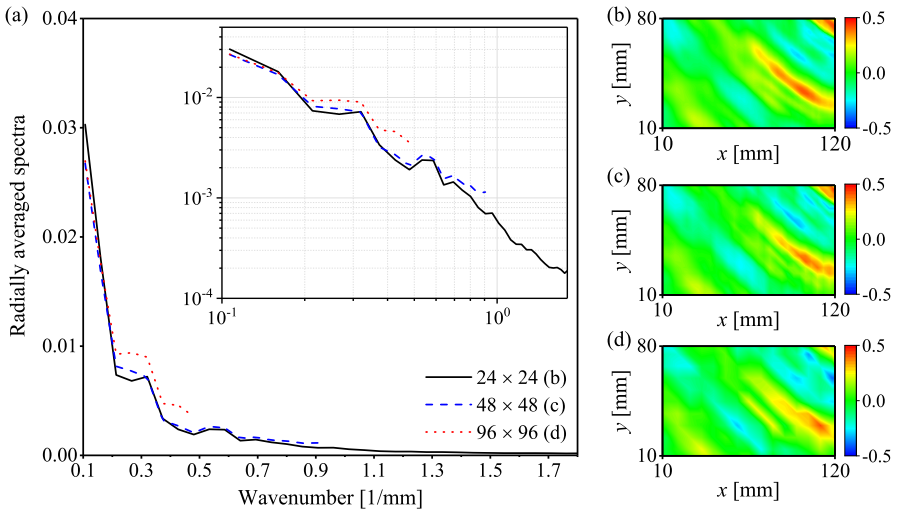

Fig. 12 (Color online) (a) Radially averaged spectra of $h(x,y)-\overline{h}$ for three interrogation window sizes. The inset shows the same data in logarithm-logarithm axes. (b–d) Contours of the same region obtained with interrogation window 24^2, 48^2 and 96^2 pixels^2, respectively.

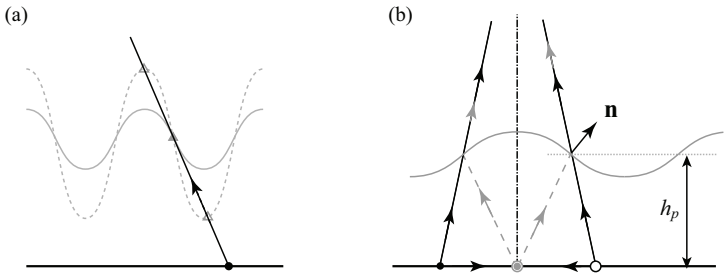

Fig. 13 The illustration of breakdown condition of the working principle: (a) Large oscillation amplitude of surface wave, where the light ray is refracted more than once as marked by hollow triangles. (b) Critical condition for formation of caustics.

in figure 12(a). The curve of 48^2 nearly collapses with that of 24^2 for moderate and large topography structures (see b and c). For an interrogation window of 96^2 pixels^2, the spectra curve deviates that of 24^2, while the noticeable difference on the surface topography can be seen in (b) and (d).

5.4 Breakdown condition of working principle

In the present method, the governing equation is physically correct provided that the light is refracted *once* on the air-liquid interface. The working principle of the present method is violated when a light ray is refracted more than once or caustics is formed. The critical condition for the former case can be depicted: For a given cosinusoidal plane wave $h(x) = h_p + \eta_0 \cos(2\pi x/\lambda)$ with wavelength λ and ampli-

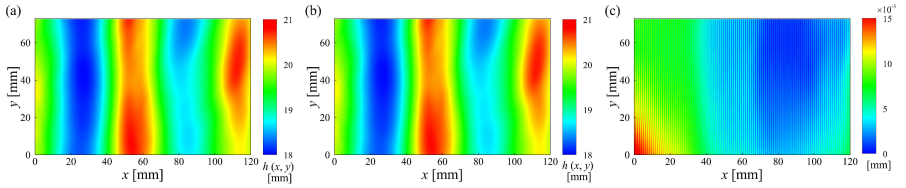

Fig. 14 (Color online) Contours of a sample of the surface ripples (the same snapshot as in figure 4 which is obtained by solving (a) the linearized equation (2), (b) equation (1) and (c) their difference.

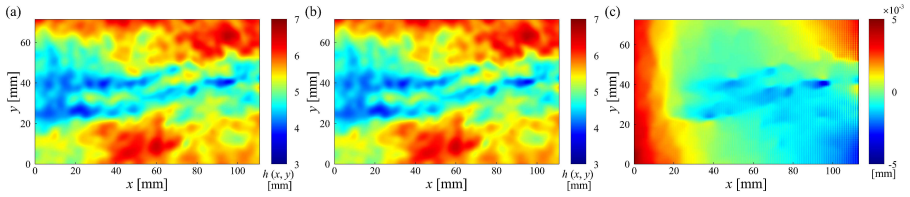

Fig. 15 (Color online) Contours of a sample of the current body (the same snapshot as in figure 7) obtained by solving (a) the linearized equation (2) and (b) equation (1) and (c) their difference.

tude η_0, the critical wave amplitude is $\eta_c = \lambda[1/4 - \beta_x/(2\pi)]$. At the same wavelength, when $\eta_0 > \eta_c$, light ray may be refracted more than once, see the dashed line in figure 13(a). For the snapshot in figure 4(c), $\lambda \approx 60$ (mm) and $\beta_x \approx 0.08$ (rad) give $\eta_c \approx 15$ (mm) > 4 (mm), and rays are refracted only once at the surface. The formation condition of the caustics depends on the viewing angle and the curvature of the surface (Gomit et al., 2013). Taking the same cosinusoidal plane wave as an example, substituting $h(x,y) = h_p + \eta_0 \cos(2\pi x/\lambda)$ into the equation 2 with $\delta\mathbf{r}(\lambda/4) \approx h_p\beta_x + \lambda/4$, the critical height is $h_{p,c} = \lambda^2/[8\pi\eta_0(1 - n_a/n_l)]$ taken the minimum of h_p. When $h_p < h_{p,c}$, no caustics is expected to be formed. However, for the very front of the current in the dam-break flow, the light rays are refracted more than once.

An *a posteriori* method was introduced in Moisy et al. (2009) to evaluate the formation of the caustics. When the largest extensional strain of the displacement field is smaller than one, no formation of caustics is expected. We used this *a posteriori* method to examine all snapshots in this study. For instance, the maximum eigenvalue for the snapshot in figure 4(c) is 0.193 (< 1) and 0.025 (< 0.15) (Moisy et al., 2009).

5.5 The effect of linearizing the governing equation

Equation (2) is obtained by linearizing the governing equation (1), e.g., taking $\tan\nabla h \approx \nabla h$ and $\tan\boldsymbol{\beta} \approx \boldsymbol{\beta}$, by truncating the second and higher order terms in their respective Taylor expansion. For example, at $\nabla h = 0.5$, $\tan(\nabla h) \approx 0.5463$ and the relative difference is about 8%. The influence of the approximation on the solution is examined in the following.

For the snapshot of the surface ripples shown in figure 4(b), the solution of the equation (2) and the equation (1) is shown in figure 14(a) and (b), respectively. The

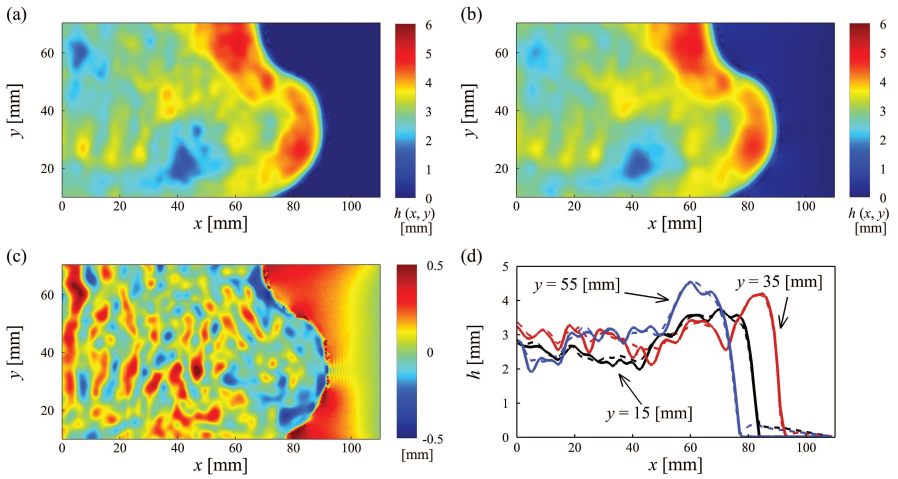

Fig. 16 (Color online) Contours of a sample of the current body (the same snapshot as in figure 10) obtained by solving (a) the linearized equation (2) and (b) equation (1) and (c) their difference. (d) Three height profiles chosen from (a) (solid lines) and (b) (dashed lines) at $y = 15$ mm, 35 mm and 55 mm.

difference between (a) and (b) is shown in (c). The mean relative difference is about 0.02%, and the standard deviation is also about 0.02%. For the snapshot of the current body shown in figure 7(a), the solution of the equation (2) and the equation (1) is shown in figure 15(a) and (b), respectively. The difference between (a) and (b) is shown in (c). The mean relative difference is about 10^{-3}% and the standard deviation is about 0.1%.

For the snapshot of the current front shown in figure 10(a), the solution of equation (2) and equation (1) have visual differences (see figure 16a and b). The difference between the two solutions, as shown in (c), gives the mean relative difference about 12% and the standard deviation of about 30%. Such difference is expected, since in the front $\nabla h \gg 1$ which violates the linearization approximation. Examination of the height profiles shows that the difference also exists downstream of the front (see figure 16d). Although the same Dirichlet boundary condition was employed for both solvers, the noise at downstream of the front for the equation (1) remains noticeable, whereas that for the linearized equation is nearly removed.

The linearized equation is accurate for $\nabla h < 1$, whereas for $\nabla h \gg 1$ (the current front), solving equation (1) is expected to give better results. However, downstream of the front there is noticeable noise albeit the Dirichlet boundary condition is imposed. In consideration that solving equation (1) takes much more computation power, the linearized equation is therefore preferred.

6 Conclusion

In this paper, we introduce a single-camera synthetic Schlieren method to measure the topography and height of dynamic free surface. In this method, displacements of the

dot patterns are attributed to both the surface height and its spatial gradients, while the reference height is not required. This method is thus applicable to flows with spatially averaged height changing in time. The dot displacements are obtained by the cross-correlation operation, while calibration is carried out to obtain the viewing angle of a camera toward the pattern object. The surface height, the only unknown in the governing equation, can be solved via a Newton-Raphson method with a proper initial guess.

We carried out two experiments to demonstrate the present method. In the experiments of surface ripples, the spatial averaged height is nearly constant. No particular treatment is performed on the boundary conditions at the borders of the computation domain. The measurement results of the present method and those of the FS-SS method of Moisy et al. (2009) agree well. In another experiment, the averaged height of the current in a dam-break problem changes with time. For the current front, a Dirichlet boundary condition is applied to the downstream boundary condition of the computation domain to amend the ill-conditioned Jacobian matrix in the Newton-Raphson solver (possibly due to the sharp current front). The Dirichlet condition is not necessary for the current body, but only when the front passes the measurement section.

The presented method is still susceptible to some limitations, when the working principle can be satisfied. Specifically, the measurement results are sensitive to the camera vibrations, a problem also reported in the FS-SS method. The vibrations change the spatial relation between the camera and the dot pattern, consequently the solutions are affected particularly on the averaged surface height. Thus, particular care is required to improve the stability of the camera as well as other components of the experimental setup. When further improvement on the setup stability is impossible, a camera with a lens of long focal length is suggested while keeping the same field-of-view being viewed, the solution is found to be less sensitive to the vibrations in our practical tests. An alternative suggested solution is to take the measurements of free surface using a portion of the camera sensor, in the meanwhile use the other portion of the sensor to record the still object which is not affected by light refraction on imaging.

Appendix

The derivation of the governing equation (1) is shown below. From the sketch in figure 17, we have

$$\begin{cases} S'P = h\ \tan(\boldsymbol{\beta}), \\ S'P' = h\ \tan(\boldsymbol{\beta}+\boldsymbol{\theta}), \\ \delta\mathbf{r} = S'P' - S'P, \\ \tan(\boldsymbol{\beta'}) = \nabla h, \\ \sin(\boldsymbol{\beta}'-\boldsymbol{\beta}-\boldsymbol{\theta})\ n_l = \sin(\boldsymbol{\beta}'-\boldsymbol{\beta})\ n_a, \end{cases}$$

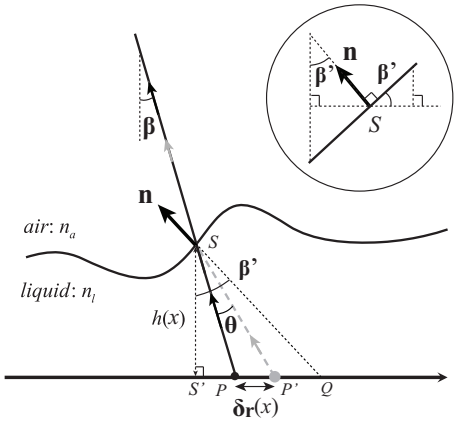

Fig. 17 Schematic of the derivation of working principle. The inset shows the zoom-in around the point *S*.

where the first four equations are obtained from geometry and the last one is from the Snell's law. Combining the above equations to eliminate $\boldsymbol{\theta}$ gives the equation (1),

$$\boldsymbol{\delta}\mathbf{r} = h \cdot \tan\left(\tan^{-1}(\nabla h) + \sin^{-1}[(n_a/n_l) \cdot \sin(\boldsymbol{\beta} - \tan^{-1}(\nabla h))]\right) - h \cdot \tan(\boldsymbol{\beta}).$$

c_t \ c_r	-3×10^{-4}	-2×10^{-4}	-1×10^{-4}	0	1×10^{-4}	2×10^{-4}	3×10^{-4}
-0.20	10.280	9.917	9.629	9.480	9.538	9.817	10.257
-0.15	9.995	9.672	9.467	9.452	9.668	10.071	10.577
-0.10	9.739	9.485	9.401	9.546	9.902	10.387	10.925
-0.05	9.534	9.387	9.457	9.754	10.209	10.737	11.285
0.00	9.406	9.403	9.632	10.046	10.557	11.101	11.647
0.05	9.386	9.542	9.903	10.388	10.924	11.469	12.006
0.10	9.486	9.785	10.234	10.755	11.296	11.835	12.359
0.15	9.697	10.100	10.597	11.130	11.667	12.193	12.704
0.20	9.988	10.454	10.972	11.505	12.031	12.544	13.040

Table 3 The averaged surface height $\bar{h}$ computed from the displacements including the camera vibration $\boldsymbol{\delta}\mathbf{r} + \boldsymbol{\delta}\mathbf{r}_{\text{vibration}}$ for the snapshot shown in figure 4c, and $\boldsymbol{\delta}\mathbf{r}_{\text{vibration}}(x,y) = c_r y + c_t$.

Acknowledgements The authors thank Katja Krömer and Peter Prengel for their technical supports. Baofang Song is acknowledged for guiding our attention to Newton methods to solve the governing equation. Huixin Li thanks for the support from China Scholarship Council (No. 201804910530). This work was supported by the Deutsche Forschungsgemeinschaft (DFG, German Science Foundation) - INST 144/464.

Conflict of interest

The authors declare that they have no conflict of interest.

c_t \ c_r	-3×10^{-4}	-2×10^{-4}	-1×10^{-4}	0	1×10^{-4}	2×10^{-4}	3×10^{-4}
-0.20	2.33	-1.28	-4.15	-5.63	-5.06	-2.28	2.10
-0.15	-0.51	-3.72	-5.77	-5.91	-3.76	0.25	5.29
-0.10	-3.05	-5.58	-6.42	-4.97	-1.43	3.40	8.75
-0.05	-5.10	-6.56	-5.86	-2.90	1.62	6.88	12.34
0.00	-6.37	-6.40	-4.12	0.00	5.08	10.51	15.94
0.05	-6.57	-5.02	-1.42	3.41	8.74	14.17	19.51
0.10	-5.57	-2.59	1.88	7.06	12.45	17.81	23.02
0.15	-3.47	0.54	5.49	10.79	16.14	21.38	26.46
0.20	-0.57	4.06	9.22	14.52	19.76	24.87	29.81

Table 4 The relative errors (%) of $\overline{h}(x,y)$ referring to the case $c_r = 0$ and $c_t = 0$ in table 3.

References

Adegok PB, Atherton W, Khaddar RMA (2014) A novel simple method for measuring the velocity of dam-break flow. WIT Transactions on Ecology and the Environment 184:23–34

André MA, Bardet PM (2014) Velocity field, surface profile and curvature resolution of steep and short free-surface waves. Experiments in Fluids 55:1709

Aureli F, Dazzi S, Maranzoni A, Mignosa P (2014) A combined colour-infrared imaging technique for measuring water surface over non-horizontal bottom. Experiments in fluids 55(3):1701

Borden Z, Meiburg E (2013) Circulation based models for Boussinesq gravity currents. Physics of Fluids 25:101301

Cobelli PJ, Maurel A, Pagneux V, Petitjeans P (2009) Global measurement of water waves by Fourier transform profilometry. Experiments in fluids 46(6):1037–1047

Dabiri D, Zhang X, Gharib M (1997) Quantitative visualization of three-dimensional free surface slopes and elevations. In: Nakayama Y (ed) Atlas of visualization, CRC Press LLC Boca Raton

Duncan JH, Qiao H, Philomin V, Wenz A (1999) Gentle spilling breakers: crest profile evolution. Journal of Fluid Mechanics 379:191–222

Engelen L, Creëlle S, Schindfessel L, De Mulder T (2018) Spatio-temporal image-based parametric water surface reconstruction: a novel methodology based on refraction. Measurement Science and Technology 29(3):035302

Fouras A, Jacono DL, Sheard GJ, Hourigan K (2008) Measurement of instantaneous velocity and surface topography in the wake of a cylinder at low Reynolds number. Journal of Fluids and Structures 24(8):1271–1277

Gomit G, Chatellier L, Calluaud D, David L (2013) Free surface measurement by stereo-refraction. Experiments in fluids 54(6):1540

Holthuijsen LH (2007) Waves in oceanic and coastal waters. Cambridge University Press

Hu H, Wang B, Zhang K, Lohry W, Zhang S (2015) Quantification of transient behavior of wind-driven surface droplet/rivulet flows using a digital fringe projection technique. Journal of Visualization 18(4):705–718

Ibrahim R (2005) Liquid sloshing dynamics: Theory and applications. Cambridge University Press

Jähne B, Schmidt M, Rocholz R (2005) Combined optical slope/height measurements of short wind waves: principle and calibration. Measurement Science and Technology 16(10):1937

Karimi G, Kawaji M (1998) An experimental study of freely falling films in a vertical tube. Chemical Engineering Science 53:3501–3512

Kolaas J, Riise BH, Sveen K, Jensen A (2018) Bichromatic synthetic Schlieren applied to surface wave measurements. Experiments in Fluids 59(8):128

Kurata J, Grattan K, Uchiyama H, Tanaka T (1990) Water surface measurement in a shallow channel using the transmitted image of a grating. Review of Scientific Instruments 61(2):736–739

Lauber G, Hager WH (1998) Experiments to dam-break waves: Horizontal channel. Journal of Hydraulic Research 36(3):291–307

Lowe RJ, Rottman JW, Linden PF (2005) The non-Boussinesq lock-exchange problem. Part 1. Theory and experiments. Journal of Fluid Mechanics 537:101

Maxworthy T, Leilich J, Simpson JE, Meiburg EH (2002) The propagation of a gravity current into a linearly stratified fluid. Journal of Fluid Mechanics 453:371–394

van Meerkerk M, Poelma C, Westerweel J (2020) Scanning stereo-PLIF method for free surface measurements in large 3D domains. Experiments in Fluids 61(1):19

Moisy F, Rabaud M, Salsac K (2009) A synthetic Schlieren method for the measurement of the topography of a liquid interface. Experiments in Fluids 46(6):1021

Morris NJW (2004) Image-based water surface reconstruction with refractive stereo. University of Toronto

Ng I, Kumar V, Sheard GJ, Hourigan K, Fouras A (2011) Experimental study of simultaneous measurement of velocity and surface topography: in the wake of a circular cylinder at low Reynolds number. Experiments in fluids 50(3):587–595

Raffel M (2015) Background-oriented Schlieren (BOS) techniques. Experiments in Fluids 56(3):60

Raffel M, Willert CE, Scarano F, Kähler CJ, Wereley ST, Kompenhans J (2018) Particle image velocimetry: a practical guide. Springer

Shin JO, Dalziel SB, Linden PF (2004) Gravity currents produced by lock exchange. Journal of Fluid Mechanics 521:1–34

Tsubaki R, Fujita I (2005) Stereoscopic measurement of a fluctuating free surface with discontinuities. Measurement Science and Technology 16(10):1894–1902

Vinnichenko NA, Pushtaev AV, Plaksina YY, Uvarov AV (2020) Measurements of liquid surface relief with moon-glade background oriented Schlieren technique. Experimental Thermal and Fluid Science 114:110051

Wieneke B (2015) PIV uncertainty quantification from correlation statistics. Measurement Science and Technology 26:074002

Zappa CJ, Banner ML, Schultz H, Corrada-Emmanuel A, Wolff LB, Yalcin J (2008) Retrieval of short ocean wave slope using polarimetric imaging. Measurement Science and Technology 19(5):055503

Zhang X, Cox CS (1994) Measuring the two-dimensional structure of a wavy water surface optically: A surface gradient detector. Experiments in Fluids 17(4):225–237